Article

Morphological and Chemical Mapping of Columnar Lithium Metal

Wesley Chang, Jeung Hun Park, Nikita S. Dutta, Craig B. Arnold, and Daniel A. Steingart*

Read Online

ACCESS | Metrics & More | Article Recommendations | Supporting Information

ABSTRACT: The development of high energy density lithium metal batteries requires the successful implementation of thin lithium metal anodes with limited excess lithium. Primary electrodeposition is a strategy for on-site production of thin lithium metal and avoids the costs and challenges of traditional lithium metal foil processing and transport. Herein we explore the interfacial parameters governing deposition of up to 30 μm uniform columnar lithium in LiF-rich environments, by investigating the effects of both the substrate/lithium and electrolyte/lithium interfaces for three common electrolytes: carbonate, fluorinated carbonate, and ether-based. By analyzing the transition to growth heterogeneity at higher current densities and later stage deposition, we confirm that improved growth uniformity is coupled with increasingly stable solid electrolyte interphases, but that this correlation differs for the three electrolytes. In comparison with conventional dimethyl carbonate, fluorinated carbonate and ether-based electrolytes exhibit fewer chemical shifts in the morphological transition region. We pinpoint the chemical origins of growth transitions in conventional dimethyl carbonate and show that close-packed columnar growth can be electrodeposited in ether-based electrolyte at 100-fold higher current densities.
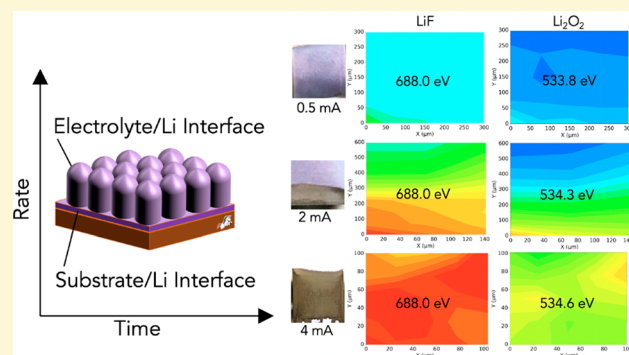
INTRODUCTION

As the most promising anode material of all metals, lithium has a high theoretical capacity (3860 mAh g^{-1}, compared with 372 mAh g^{-1} for conventional graphite anodes) and a low negative redox potential (−3.04 V vs standard hydrogen electrode).[1−5] In recent years, there has been an increasing emphasis placed on limiting lithium content in a secondary lithium metal battery, as any excess inventory in the anode beyond the cathode capacity results in a loss in energy density.[6] A practical thickness of less than 30 μm is required to reach targeted cell-level energy densities of beyond 500 Wh kg^{-1}, a primary goal of the U.S. Department of Energy Battery500 program and a specific energy requirement necessitated by the growing electric vehicle energy-storage market.[7] This assumes the use of a state-of-the-art cathode, minimal excess electrolyte and inactive materials, and a significantly lower lithium metal thickness. The challenge here lies in the development of thin lithium foil through conventional extraction and roll-to-roll processing, due to increasing cost and energy-intensiveness of mechanically deforming lithium metal, which tends to experience ductile failure and loss of uniformity at such low thicknesses. Alternatively, methods such as vapor deposition, sputtering, or primary electrodeposition may offer new pathways for synthesis of uniformly thin lithium metal.[8−10] The starting inventory of lithium metal may be constructed as an anode on the copper current collector or stored in the cathode and cycled on a bare current collector in an "anode-free" configuration.[11,12] For either case, an improved under-

standing of the governing parameters which dictate uniform plating will aid in the development and scale-up of limited lithium metal content batteries.[13,14]

Previous demonstrations indicated the possibility of producing uniform lithium metal via primary electrodeposition, with the lithium source from a lithium carbonate-based aqueous solution.[8,9] Pretreating the copper current collector with acid and deionized water solution was shown to initiate the formation of a LiF layer on the substrate surface, which promotes a uniform close-packed columnar morphology and improves coulombic efficiency over that of an untreated Cu substrate.[9,17] This is akin to several other methods in the literature, including the addition of trace amounts of water or CsPF$_6$ additives to conventional carbonate electrolyte.[15−18] The combined properties of high shear modulus and high surface lithium diffusivity of LiF, as studied by Archer and co-workers, presumably modulate the uniform growth of lithium nuclei in both the lateral and vertical direction.[19−24] This is significant because it indicates the possibility of dendrite growth mitigation in conventional carbonate electrolytes without major modification to existing cell design. From
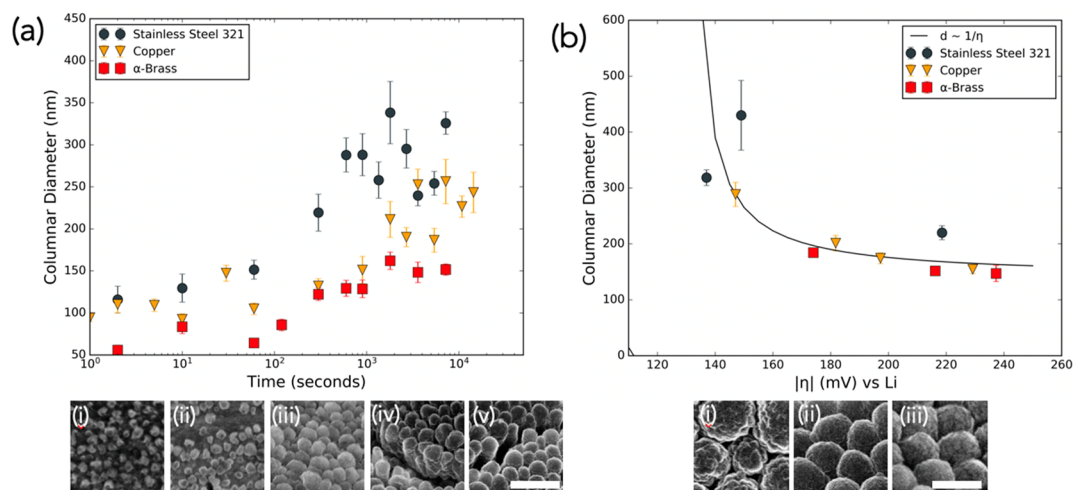
Figure 1. (a) Average Li column diameter as a function of time (s), depicting nucleation and growth behavior on various metal substrates at a current density of 0.5 mA cm^{-2}. (b) Average column diameter as a function of overpotential (mV vs Li/Li$^+$), depicting inverse relationship between growth size and applied current density, with all samples measured at 1 mAh cm^{-2}. Corresponding SEM images depict columnar growth at various points in the plots, with scale bars corresponding to 500 nm. Deposition was carried out on acid treated stainless steel 321, copper (99.95%), and brass (63 wt % Cu, 37 wt % Zn).

recent research, a fluorinated interphase brings clearly tangible benefits as summarized by Meng et al., but a complete understanding of LiF distribution in the solid electrolyte interphase (SEI) as a function of current density and charge passed is lacking.[25] The initial nucleation of Li on various substrates has also been well studied by Cui et al., but not so much the later stage growth.[14,26] Is columnar growth inherent in low current density high-LiF-content interphases regardless of electrolyte? As Dasgupta et al. pointed out, the following fundamental research questions still need to be answered: "*what are the origins of the spatial/temporal variations in chemical composition and impedance of the SEI... what are the chemical and mechanical origins of hot spots where SEI fracture and mossy dendrite nucleation occur?*"[40]

This Article investigates the relationship between uniform column morphology and the substrate/lithium and electrolyte/lithium interfaces, comparing three commonly studied electrolytes for lithium metal: carbonate-based (1 M LiPF$_6$ in dimethyl carbonate, or DMC), fluorinated carbonate (1 M LiPF$_6$ DMC + 10% fluoroethylene carbonate, or FEC), and ether-based (1 M LiTFSI in 1,3-dioxolane:1,2-dimethoxy-ethane, or DOL:DME, 1:1 by volume). While the substrate overpotential is known to have an inverse correlation with initial nuclei size,[14] we show the electrolyte exerts greater influence on long-term growth diameter. Failure mode analysis comparing the above-mentioned three electrolytes shows that close-packed columnar morphology deposits at higher rates in DOL:DME electrolyte before growth become rough and/or dendritic. We believe this is related to the chemical stability of the resulting SEI layer. While lithium metal deposition occurs well outside the stable voltage window of carbonate electrolytes, (<1.3−0.8 V vs Li), it just exceeds the stability limits for ether electrolytes (<0 V vs Li).[5] The lower voltage range for reduction product decomposition of ethers was well reviewed by Winter et al.[5] and also by Etacheri et al. for Li-ion batteries.[28] Fluorinated carbonates have also been shown to form polymeric carbonate decomposition products, resulting in a thinner and tougher SEI layer.[23] Building upon prior literature on the higher cycling efficiency of fluorinated solvent and ether-based solvent, we show that (1) primary electro-

deposition of columnar morphology sustains in DOL:DME electrolyte at over 50 mA cm^{-2} as compared with 0.5 mA cm^{-2} for DMC; and (2) spatial mapping of morphology and SEI chemical composition indicates FEC and DOL:DME electrolytes form relatively stable SEIs even for mossy, ramified, or dendritic lithium. FEC and DOL:DME electrolytes did not experience any surface growth protrusions on columnar deposition, unlike the case for DMC. Growth protrusions in DMC electrolyte were further probed by cryogenic transmission electron microscopy (cryo-TEM) analysis, which confirms that the chemical changes are localized on these growth protrusions.

■ RESULTS AND DISCUSSION

Lithium/Substrate Interface. A complete study of electrodeposited lithium metal requires understanding of both the lithium/substrate and lithium/electrolyte interfaces. On the lithium/substrate interface, copper metal is often the current collector, largely the legacy of commercial lithium-ion batteries. Copper has high electrical conductivity and is generally stable against the graphite negative electrode. Metals which alloy readily with lithium are suboptimal because of the mechanical fracture that may occur during alloying/dealloying; this includes silicon, platinum, zinc, and aluminum.[26] Therefore, most studies in the lithium metal battery literature continue to use copper as a deposition substrate.[29] However, lithium is soluble to a significant 22 atom % in copper at 298 K according to equilibrium phase measurements.[30]

The initial nucleation of lithium occurs on the lithium/substrate interface, and we study the relationship between the initial nucleation and subsequent long-term growth. We investigated the effect of the substrate overpotential on columnar growth and hypothesized the growth of larger column diameters would decrease the electrochemically active surface area of the deposited columns and reduce side reaction rate with the electrolyte. Since the substrate type affects the deposition overpotential, substituting copper for another metal less hostile to lithium nucleation should be expected to increase the critical nuclei size according to heterogeneous nucleation theory. This is expected to result in slower
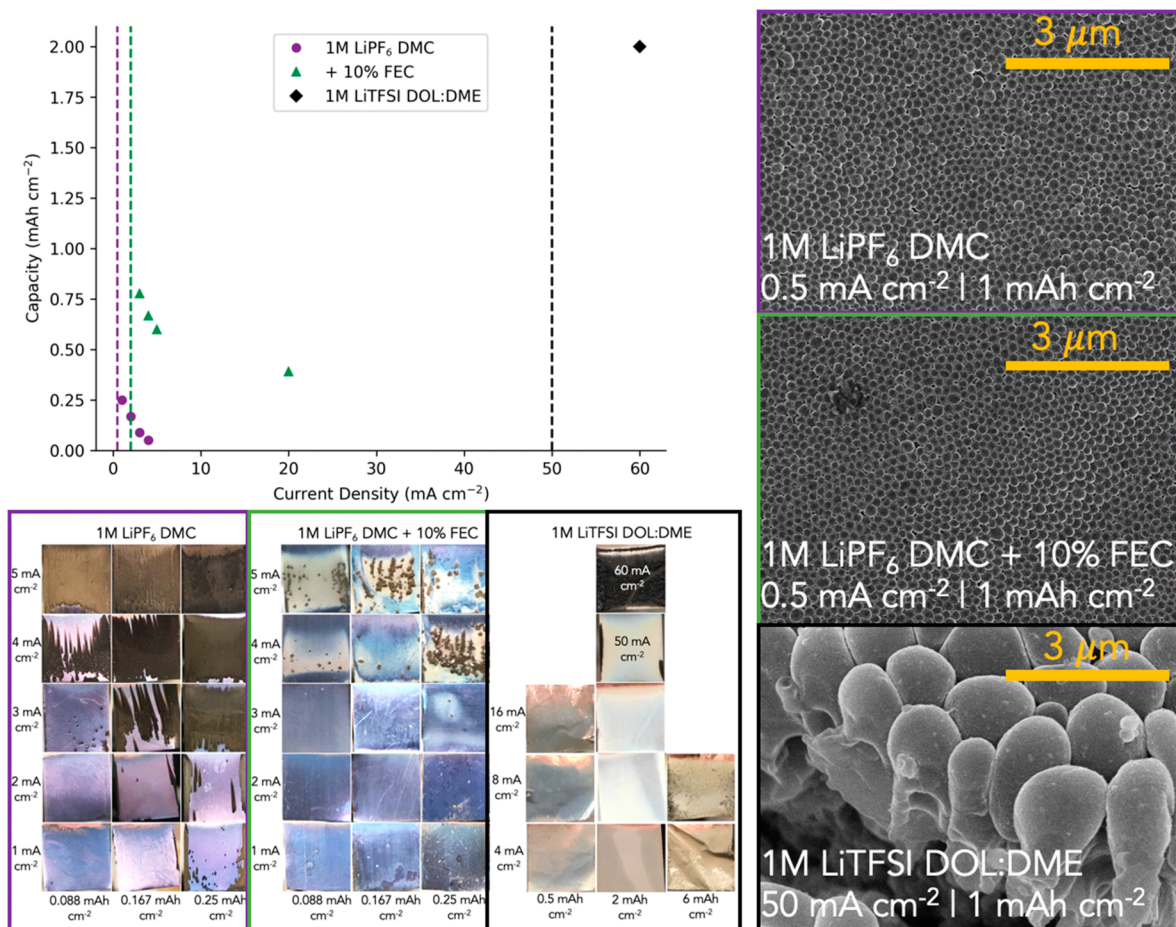
Figure 2. Areal capacities (mAh cm^{-2}) and areal current densities (mA cm^{-2}) at which transition from close-packed columnar Li to nonuniform Li growth occurs in 1 M LiPF$_6$ DMC, 1 M LiPF$_6$ DMC + 10% FEC, and 1 M LiTFSI DOL:DME. Values are estimated from individual plating experiments, with representative optical images demonstrating clear morphological transition from purple/columnar to black/nonuniform. SEM images of examples of close-packed columnar growth at lower current densities are shown. Note the significantly larger columns in 1 M LiTFSI DOL:DME even at a high current density of 50 mA cm^{-2}. Columnar diameters in 1 M LiPF$_6$ DMC with or without 10% FEC are similar in size. Optical micrographs are 1 cm × 1 cm.

electrolyte reaction rate and hence larger columns during late-stage deposition.

Figure 1 details the relationship between the type of substrate and the measured column growth diameter. Figure 1a details the growth dynamics over time for each of the three tested substrates: stainless steel 321, copper, and brass, with the column diameters measured at various time intervals at 0.5 mA cm^{-2}. These three substrates were chosen for their relative chemical stability during Li plating, as they are not known to alloy substantially with lithium. Copper and stainless steel have been widely used in the literature for lithium plating studies,[31] and planar brass foil appears stable. To confirm the stability of planar brass, the plating voltage profiles and X-ray diffraction (XRD) spectra of the columnar Li on brass are depicted (Figure S1). The plating overpotential profiles are similar for brass vs copper, in both 1 M LiPF$_6$ DMC and 1 M LiTFSI DOL:DME (Figure S1a). Both copper and brass exhibit an initial nucleation spike along with electrolyte reduction/SEI formation, followed by long-term growth. Platings in 1 M LiPF$_6$ DMC took longer to reach underpotential deposition (<0 V vs Li) because of more significant electrolyte reduction. On the other hand, this can be contrasted with the voltage profile for Li deposition on Zn metal, which involves an initial alloying step and no nucleation peak. XRD shows that LiZn

can be detected if Li is plated onto Zn metal; however, the same LiZn peaks are absent for Li deposited onto brass (Figure S1b). Even though several recent studies have been reported on brass substrates for improved Li deposition and cycling, they all involved some form of subsequent dealloying or heat treatment procedure in order to create a 3D mesh structure[32] or to coat the surface with Zn or ZnO.[33] This would result in a material drastically different than that of planar rolled brass foil with an unmodified surface. For these reasons, the three substrates copper, stainless steel, and brass were chosen to investigate the substrate/lithium interfacial impact on columnar Li growth dimensions.

Figure 1b details the correlation between column diameter and overpotential vs reference lithium, with the overpotential changed by changing the applied current density, normalizing for 1 mAh cm^{-2} of charge passed. As expected, there is an inverse relationship between column diameter and overpotential vs reference lithium. The brass current collector exhibits a higher overall overpotential vs reference lithium, and hence results in lower average column diameter. For example, the initial nuclei grow to a steady-state column diameter of 151.6 ± 13.4 nm for brass, as opposed to 325.9 ± 26.7 nm for stainless steel 321 (Figure 1a).

Therefore, the long-term column diameters are affected by the substrate overpotential, which depends on the type of substrate used. From a series of scanning electron microscopy (SEM) images taken at various time intervals of deposition, *ex situ*, there are two different growth stages. The first stage involves enlargement of the deposited nuclei, which occurs for the first ~15 min of plating. For a higher overpotential substrate such as brass, there are more nuclei and they have smaller diameters than the nuclei of a lower overpotential substrate such as stainless steel 321 (Figure S2). This makes sense given a similar faradaic efficiency for each substrate; the total amount of Li plated with the same amount of charge passed should be equivalent. The second stage involves vertical columnar growth, with the diameters having reached a steady-state value. Vertical columnar growth presumably initiates when the tips of the deposits reach far enough into the electrolyte to become the preferential sites for subsequent deposition. Despite the suggested theory that larger nuclei impinge upon each other and force growth in the vertical direction, the data presented here agrees with the former hypothesis, as columnar growth is observed even before a completely close-packed layer is formed. For example, a comparison of the deposition at 22.5 and 90 min in Figure S2a indicates that while the growth at 22.5 min is not yet completely close-packed as compared with 90 min, growth in the vertical direction is already starting to appear. The lithium has a choice of depositing on the sides or on the substrate, but instead it deposits on the top.

The evaluation of columnar lithium growth on various substrates agrees with existing studies on lithium metal nucleation and growth relating overpotential to nuclei size. There are two types of growth: the initial enlargement of deposited nuclei and the vertical growth of close-packed columns. The columnar growth can be obtained irrespective of substrate type, and is within an order of magnitude in size, with diameters inversely correlated with overpotential. Despite this inverse correlation, the relative similarity of the various columnar diameters suggests that the more dominant interface for controlling the bulk morphology and subsequent cycling efficiency lies at the lithium/electrolyte boundary. As will be described in a later section, we also show that the subsequent cycling efficiency is independent of column diameter; for example, brass appears to cycle better than stainless steel despite columns that are 50% smaller.

Lithium/Electrolyte Interface. The lithium/electrolyte interface is an order of magnitude thicker than the few nanometers thick interface between the lithium and substrate and is composed of the ~10−50 nm SEI layer formed from side reactions between deposited lithium and the electrolyte salt/solvent.[34,35] The lithium/substrate interface has been recently explored in the literature with separate measurements by X-ray photoelctron spectroscopy (XPS) depth profiling[9] and cryo-TEM[36] both indicating an ~5−8 nm thick interface on copper. Peled and Menkin had also previously measured the lithium/electrolyte interface (SEI) for various anode configurations by time-of-flight secondary ion mass spectrometry and XPS, ranging from 7 to 35 nm on graphite, 22 to 72 nm on SiNWs, and 10 nm for Li/sulfur.[37]

In order to investigate the effects of varying electrolyte on the columnar morphology and related SEI chemical composition, an array of plating images at increasing current rates and deposition thicknesses (plating capacity) was taken (Figure 2). This series of images depicts the bulk plating morphology as a function of current density and capacity and shows optically where the transition from uniform growth to nonuniform growth occurs. This transitional area was then analyzed in full detail, using XPS spatial mapping to determine surface chemical composition as a function of growth morphology observed under the SEM. Growth "failure" is defined as the loss of close-packed morphology before 6 mAh cm^{-2} lithium is deposited (which translates to roughly 25−30 μm thickness accounting for non-faradaic losses). Based on the optical micrographs, the areal capacity at a specific areal current density at which the growth transition occurs can be approximated and plotted, as shown. The trends indicate that higher current densities result in faster transition to nonuniform morphology and that there is a maximal current density at which columnar growth can be observed indefinitely (dotted vertical lines in Figure 2). For example, columnar growth was observed up to 24 mAh cm^{-2} in 1 M LiPF$_6$ DMC at 0.5 mA cm^{-2}.

Failure Mode of 1 M LiPF$_6$ DMC. A failure analysis of the conventional carbonate electrolyte (1 M LiPF$_6$ DMC) indicates that, for the 6 mAh cm^{-2} deposited capacity, the maximum current density that can sustain the close-packed columnar morphology is 0.5 mA cm^{-2}. From the optical images, it can be observed that increasing the current density beyond 0.5 mA cm^{-2} results in a decrease in the amount of time it takes for nonuniform deposits to appear (Figure 2). Plating at 2 mA cm^{-2} results in a nonuniform region appearing at the edges, whereas plating at 4 mA cm^{-2} results in a completely nonuniform surface. Optically, the nonuniform regions appear as rough black deposits on the otherwise smooth mirrorlike surface. These spots tend to appear with greater concentrations near the edges of the substrate, due to geometric edge effects of the electric field.[38] Under high magnification SEM, the boundary layer between uniform and nonuniform regions is observed (Figure S3). A closer investigation of this transition region shows that the nonuniform growth initiates on preexisting lithium deposits. On certain portions of the columns, bright charged areas appear and protrude outward. These protrusions gradually become more densely distributed on top, with the underlying columnar morphology remaining. Compared with 1 M LiPF$_6$ DMC, the addition of 10% FEC increases the maximum current density at which uniform columnar morphology persists (Figure 2). In 10% FEC, 10 μm (6 mAh cm^{-2}) can be plated at 2 mA cm^{-2}, an increase over 0.5 mA cm^{-2} for DMC, even though the columnar morphology and diameters are indistinguishable from the DMC case (Figure 2). We emphasize that this maximum current density is not the classical limiting current density due to mass transport limitations, but instead a measured current density at which a growth transition from close-packed columnar to nonuniform deposits is observed. Linear sweep voltammetry was conducted in the three electrolytes in order to estimate the limiting current density (Figure S4). As demonstrated by the plots of logarithmic current density vs *iR*-corrected overpotential (with ohmic resistance correction estimated by electrochemical impedance spectroscopy, depicted in Figure S5), 1 M LiTFSI DOL:DME exhibits a high j_{lim} of around 86 mA cm^{-2}, 1 M LiPF$_6$ DMC + 10% FEC a j_{lim} of 72 mA cm^{-2}, and 1 M LiPF$_6$ DMC a j_{lim} of 40 mA cm^{-2}. The plating current density regimes for close-packed columnar morphology are significantly lower than j_{lim} in the carbonates (0.5−2 mA cm^{-2}) and about half the limiting current in 1 M LiTFSI DOL:DME. As will be shown in the
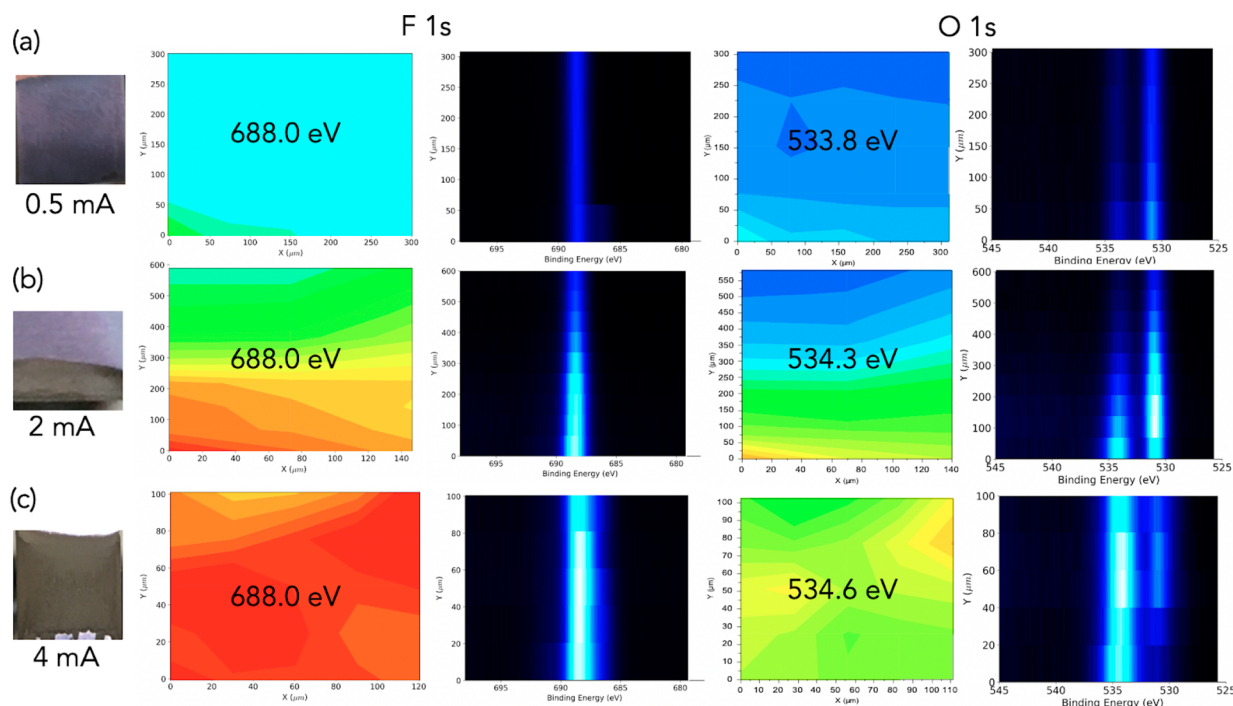
Figure 3. XPS 2D area maps and corresponding line scans for both F 1s and O 1s scans, for columnar Li deposition in 1 M LiPF$_6$ DMC, at (a) 0.5 mA cm^{-2}, (b) 2 mA cm^{-2}, and (c) 4 mA cm^{-2}. The transition region from columnar to nonuniform at 2 mA cm^{-2} clearly shows an intensity gradient for both F 1s and O 1s scans, indicating an increase in LiF% and Li$_2$O$_2$% in the nonuniform region. The F 1s scan maps are shown for 688.0 eV binding energy, which correlates with the LiF peak, and the O 1s scan maps are shown for the Li$_2$O$_2$ peak, which is around 534 eV.

next section, extensive XPS spatial mapping coupled with cryogenic electron microscopy of surface growth asperities provides evidence that surface SEI chemical heterogeneity plays a predominant role in deposition morphology, especially since the plating current densities applied here are much lower than the system limiting current density. Loss of chemical homogeneity suggests greater variation in the SEI, and higher possibility of nonuniform growth due to localized defect sites.

Compared with the carbonate electrolytes, 1 M LiTFSI DOL:DME (ether-based) electrolyte exhibits a significantly higher maximum current density for columnar growth. While the same lower current densities of 0.5 and 2 mA cm^{-2} resulted in gray deposits with nonuniform, but close-packed, columns (Figure S6), increasing the current density to greater than 4 mA cm^{-2} resulted in more uniform growth. When viewed via SEM, the gray deposits were composed of columnar growth that is nonuniform in height, whereas the purple deposits at greater than 4 mA cm^{-2} were composed of more uniformly distributed columns (Figure 2). During the failure mode analysis, columnar growth was obtained at current densities ranging from 4 mA cm^{-2} up to 60 mA cm^{-2}, at which point nonuniform morphology initiated. Considering that most studies of ether-based electrolytes consist of cycling current rates 10-fold greater than those of carbonates (10 vs 1 mA cm^{-2}), a 100-fold increase is more significant though perhaps expected for a single primary protocol.[39] This results in the growth of 30 μm columns in less than 8 min, as opposed to 3 h for 10% FEC or 12 h for DMC. It should be mentioned that, even at 60 mA cm^{-2}, the current density regime is not diffusion limited.

Because the length scale of the transition region for the DMC case (from black to purple) is on the order of hundreds of micrometers, XPS spatial mapping is a suitable technique for

determining corresponding variations in the surface chemical composition. XPS provides high depth resolution, imaging the top 10 nm of the surface along with depth profile capabilities, and sufficient lateral resolution, with an achievable spot size of 30 μm. As shown, the morphological transition from columns to nonuniform protrusions correlates with a similar transition in surface chemical composition. We specifically focused on analyzing compositional differences of the inorganic species of the SEI, specifically LiF, Li$_2$O, and Li$_2$O$_2$, because quantitative analysis of the full scans revealed that these were the predominant compositions of our LiF-rich SEI. Outer SEI composed of soluble and organic species may have been further minimized by copious rinsing and drying of the substrates before characterization; alkyl carbonates and other organic species were still observed in the C 1s scans, though the low spot size and relatively fast scan rate for full area mapping resulted in noisier low binding energy scans.

In Figure 3, the F 1s and O 1s area maps of a completely homogeneous surface at 0.5 mA cm^{-2} (Figure 3a) are compared with those of a completely nonuniform surface at 4 mA cm^{-2} (Figure 3c), and also with an intermediate current density at 2 mA cm^{-2} (Figure 3b) that led to a transition, all for 1 M LiPF$_6$ DMC. The area maps, which consist of many point scans in a grid on a desired region, plot the relative peak intensity at a specific binding energy, which corresponds to the presence of a specific chemical state. For the F 1s area maps, the 688.0 eV peak corresponding to LiF is shown.[27,41−42] The fully uniform plating at 0.5 mA cm^{-2} is depicted in Figure 3a and correlates with a relatively lower intensity LiF peak. The transitional plating at 2 mA cm^{-2} in Figure 3b correlates with a gradual increase in intensity toward the nonuniform growth. The fully nonuniform growth at 4 mA cm^{-2} in Figure 3c correlates with a relatively higher intensity LiF peak. This is
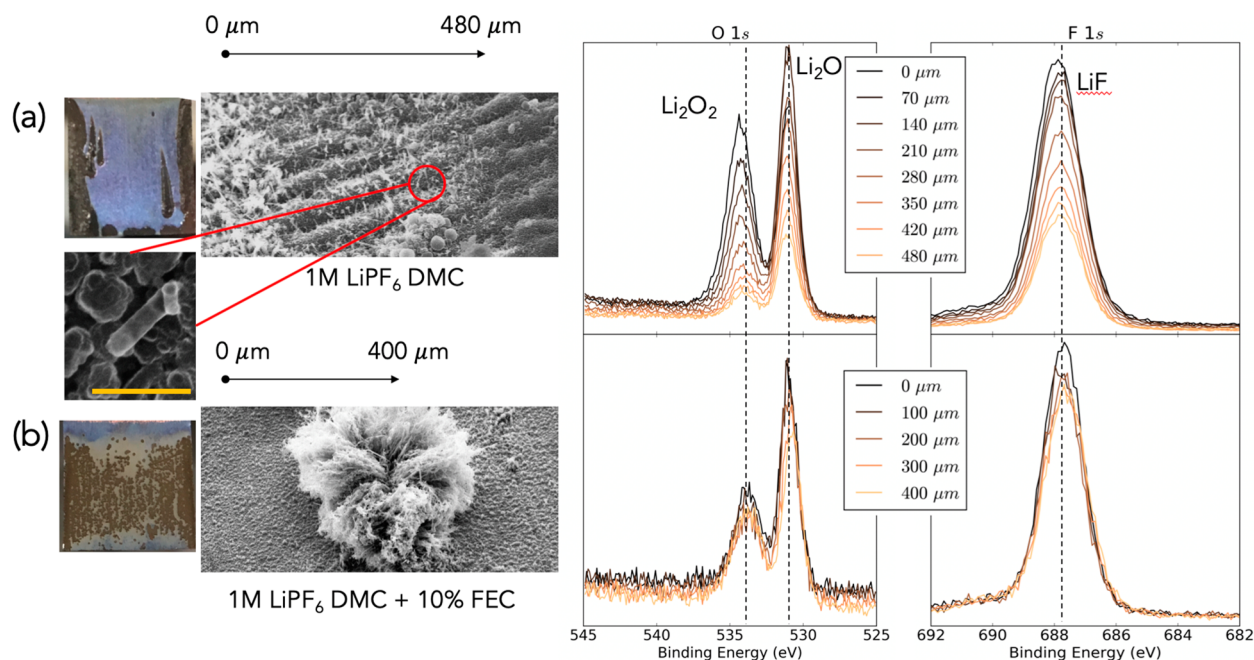
Figure 4. Failure mode analysis of uniform/nonuniform transition regions comparing (a) 1 M LiPF$_6$ DMC and (b) 1 M LiPF$_6$ DMC + 10% FEC. The current density and capacity parameters for the transition region were determined by analyzing the conditions plated shown in Figure 1. For (a), a line scan was taken with step size of 70 μm and total distance of 480 μm from the nonuniform to uniform columnar regions. For (b), a line scan was taken with step size of 100 μm and total distance of 400 μm from the uniform to nonuniform regions. This transition occurs gradually in (a) and suddenly in (b). Higher resolution SEM image indicates growth asperity on underlying column, with the scale bar corresponding to 300 nm.
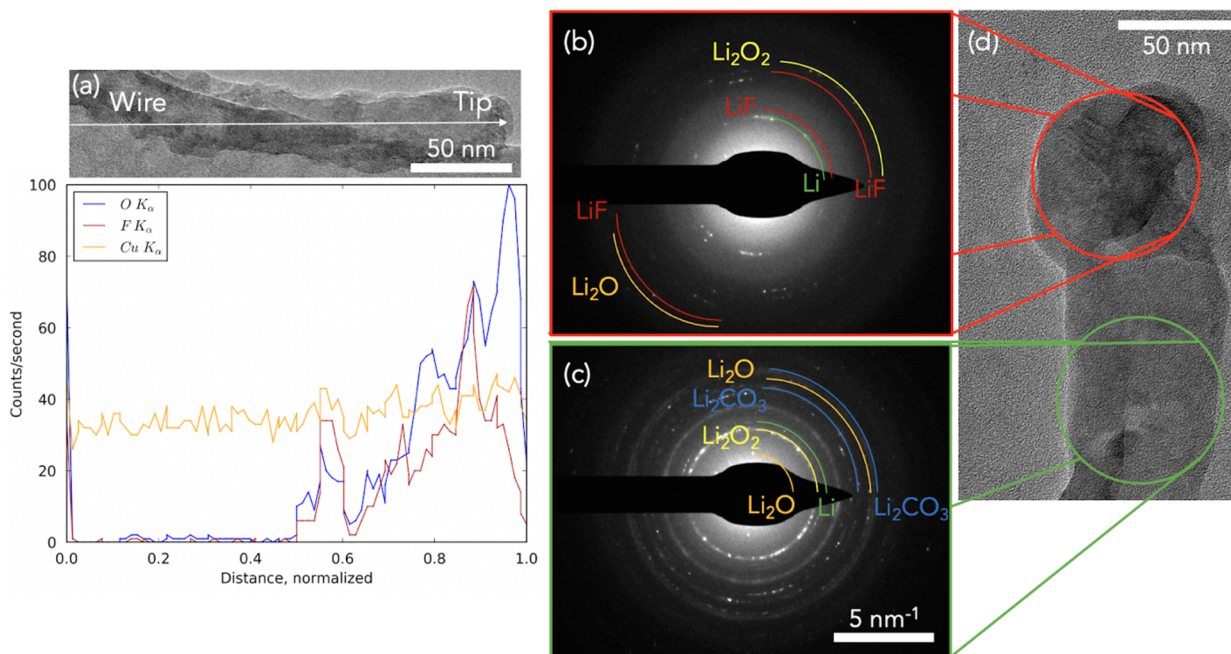

Figure 5. Cryo-TEM analysis of individual protrusions in uniform/nonuniform transition in 1 M LiPF$_6$ DMC. High resolution SEM images show that failure occurs due to protrusions growing on top of columnar lithium deposits, possibly due to defect sites generated from higher local current densities. These protrusions are harvested onto a TEM grid and kept at ~100 K in a liquid nitrogen cryo-holder for TEM imaging and diffraction. (a) An EDS line scan from the base of the deposited wire to the tip indicates higher detected quantities of fluorine and oxygen species near the tip, where the protrusion is more exposed to electrolyte during plating and possibly resulting in more SEI degradation. (b) Tip and (c) base of wire electron diffraction patterns, with regions indicated in the image in (d). Failure mode analysis is important to determine where nonuniformity exactly occurs, and specifically which chemical compounds are formed in the SEI at these locations. Diffraction peaks were indexed using JC-PDS catalog #45-1460 (for LiF), #15-0401 (for Li), #09-0359 (for Li$_2$CO$_3$), #25-0486 (for LiOH*H$_2$O), and #12-0254 (for Li$_2$O).

also demonstrated by a gradual decline in intensity of the adjacent line scan, in Figure 3b. Likewise, the O 1s area maps

indicate that the morphological transition from nonuniform to uniform columns is followed by a decrease in intensity of the

Li_2O_2 peak at 534.3 eV.[40] The adjacent line scan indicates that both the 534.3 eV Li_2O_2 peak and the 530.5 eV Li_2O peak decline in intensity, with the Li_2O becoming the more dominant peak in the uniform growth case. The peaks in the C 1s scan also showed slight shifts to higher binding energy, though suffered noise issues due to the relatively faster scan rate required for completing the entire spatial map in a reasonable amount of time. For these long duration spatial mapping, 1 min of depth profiling was carried out before each point scan in order to remove monolayer surface contaminants that may have built up within the XPS chamber.

The transition from black- to purple-colored plating can be viewed more closely in Figure 4a. The SEM image shows that the interface between black- and purple-colored plating is around 500 μm. Within this transition region, the higher resolution SEM image shows that the nonuniformity initiates as growth asperities on existing columns (see also Figure S3). The ~50 nm length scale of these growth asperities make them appropriate for further characterization in the S/TEM using a cryo-holder.[43−46] Cooling to 100 K (−170 °C) with liquid nitrogen stabilizes these growth protrusions long enough to allow for electron diffraction and energy dispersive X-ray spectroscopy (EDS) analysis. Contamination and reaction due to ambient atmosphere is minimized by harvesting the protrusions onto a copper TEM grid and loading into the cryo-holder in the Argon filled glovebox; the holder was then vacuum sealed before transferring from the glovebox to the TEM. The EDS line scan, taken in scanning transmission electron microscopy (S/TEM) mode, indicates that these growth protrusions are predominantly composed of fluorine and oxygen (apart from lithium, which cannot be detected by EDS), with the concentration increasing near the exposed tips (Figure 5a). This may be a result of closer proximity to the electrolyte during deposition, and thus higher reactivity at the tips. Electron diffraction analysis of several different protrusions provides a general qualitative assessment of their chemical composition. For each protrusion, diffraction peaks corresponding to Li^0, LiF, Li_2O, Li_2O_2, Li_2CO_3, and LiOH·H_2O were observed, indexed using the normalized integrated intensity of each diffraction pattern (Figure S7) and compared with the highest intensity peaks in JC-PDS reference files. These are the usual chemical species present in the SEI, with the exception of LiOH·H_2O which may have been a product of sample preparation contamination. Another peak was present for all samples at a d-spacing of 1.7 Å which could not be matched with any reference peaks and may have been due to another decomposition product. Additionally, all diffraction patterns had both polycrystalline and amorphous character, pointing to the existence of both types of SEI on the protrusions, with the amorphous material most likely consisting of other carbonate decomposition products not observed in the F 1s and O 1s XPS maps.

The nature of these growth asperities must be compared with other varieties of nonuniform lithium deposits explored in the literature. Cryo-TEM investigations on lithium deposits have divided results, with one report demonstrating clear lattice fringes and single crystalline dendrites,[46] but yet another report exhibiting amorphous lithium growth during the initial nucleation-dominated regime.[44] Both of these reports involved lithium deposits grown directly on the Cu TEM grid, whereas in the current case, growth asperities were observed on localized regions of preexisting lithium columns. We believe that since the growth asperities occur on preexisting columnar

Li and must be extracted onto a TEM grid, as following a procedure by McDowell et al.[47] for lithium oxide nanowires, the process may cause some surface passivation to occur such as the presence of LiOH·H_2O. However, surface passivation does not account for the other polycrystalline components detected by TEM diffraction, which indicate that these growth asperities are SEI-rich rather than purely metallic lithium. Growth on preexisting columnar lithium due to local defects and SEI degradation may drastically alter the amorphous/polycrystalline character of these asperities. Electron microscopy analysis of growth asperities of a few different samples obtained at slightly different conditions all showed mixed amorphous/polycrystalline properties. The amorphous to crystalline transition for lithium deposits either during nucleation or subsequent growth is an interesting avenue for further exploration.

Classic Sand's diffusion-limited dendrite growth mechanisms have been applied to lithium dendrite growth by Bazant et al.,[48] but the current process does not operate in the mass transfer controlled regime. The growth asperities are only observed in 1 M $LiPF_6$ DMC and at relatively low current densities of <4 mA cm^{-2}, which is far below the limiting current density of >100 mA cm^{-2}. Even in 1 M LiTFSI DOL:DME, the plating current of 50 mA cm^{-2} which results in columnar deposition is also less than half the j_{lim}. At > 60 mA cm^{-2}, growth asperities were not observed, but rather a sudden transition to thick fibril-like deposition that appears as a smooth gray film. On the other hand, Yamaki et al. proposed a stress-driven growth model where stress builds up between the SEI and the underlying lithium substrate.[49] Yet in another report, Steiger et al. suggested an alternative growth mechanism driven by insertion at crystalline defects behind an inactive structure.[50]

These growth asperities appear to be mechanistically analogous to the model proposed by Steiger et al.[50] The combination of selected area electron diffraction and EDS line scans makes it clear that these growth protrusions are SEI-rich, especially near the tips. In Figure S3c, a subsequent stripping protocol shows that while the underlying columns strip away from the sides, the growth protrusions do not, pointing toward their electrochemical inactivity. As the preexisting underlying columnar lithium would not be expected to experience much of a change in their SEI chemical composition, it makes sense that any changes are localized to the surface growth protrusions. From the combination of cryo-TEM and XPS spatial mapping, it seems that the shift to higher binding energy species (i.e., more of Li_2O_2 rather than Li_2O) observed at the transition in XPS are localized to these protrusions. At the same time, the electron diffraction patterns for various growth protrusions are not identical and show slightly different features, pointing to the variations in chemical states. This pinpoints the origin of chemical heterogeneity in the poor performing 1 M $LiPF_6$ DMC electrolyte resulting in growth asperities and loss of electrochemically active lithium.

Failure Mode of 1 M $LiPF_6$ DMC + 10% FEC. On the other hand, a different failure mechanism was observed for the case with 10% FEC additive in 1 M $LiPF_6$ DMC. FEC is widely known to improve the SEI stability, aided by the formation of both the LiF decomposition product as well as polymeric decomposition products in the SEI.[21] While the maximal current density for close-packed columns in DMC is 0.5 mA cm^{-2} for formation of 30 μm lithium, the maximal current density for columns in DMC + 10% FEC is 2 mA cm^{-2}. This
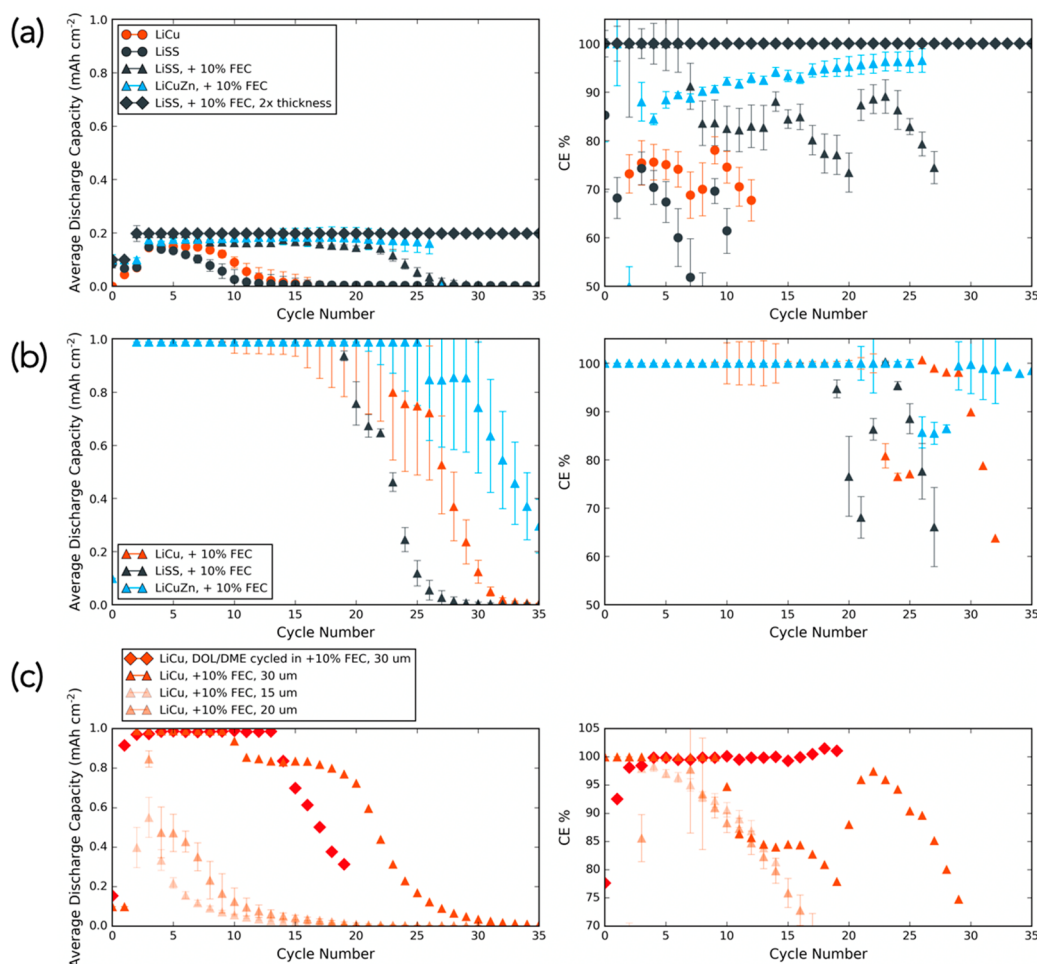
Figure 6. (a) Average discharge capacity and CE% of 1 mAh cm^{-2} (5 μm) columnar Li (at low current rate conditions of 0.1 mA cm^{-2}, 0.2 mAh cm^{-2}) in coin cell configuration vs delithiated LFP cathode. Small differences are observed for substrate type, with a clear improvement of CE% upon addition of 10% FEC. The most significant impact came from doubling the amount of starting Li (diamond markers). LiCu = copper, LiSS = stainless steel 321, LiCuZn = brass. (b) Scale up of several substrates with 10% FEC, using 30 μm thick columnar Li, and cycled at 0.5 mA cm^{-2}, 1 mAh cm^{-2}. (c) Correlation between the thickness of deposited columnar Li and cycling performance for 1 M LiPF$_6$ DMC + 10% FEC on Cu substrate. Here, 30 μm columns in 10% FEC are comparable with 30 μm columns in DOL:DME (also cycled in 10% FEC, orange diamond markers).

suggests deposition of 30 μm in 3 h (to obtain 6 mAh cm^{-2}), rather than 12 h in DMC. In observing the SEM image in Figure 4b, it appears that the transition to nonuniformity causes bulk disruption of the columnar morphology. Instead of anisotropic protrusions deposited on the underlying columns, the nonuniformity is more localized and causes disturbance of the entire length of the columns. In other words, the interface between uniform columns and nonuniform growth is sharper, and in the nonuniform region the bulk columns are affected. This "peeling away" effect suggests mechanical instability of the entire deposit. In contrast with the XPS results for DMC, the XPS line scans indicate no change in surface chemical species despite these morphological disruptions, with both the F 1s and O 1s scans showing almost identical relative peak intensities during the transition (Figure 4b).

Failure Mode of 1 M LiTFSI DOL:DME. Third, we analyzed the transition to failure for ether-based electrolyte (1 M LiTFSI DOL:DME). The initial low current density plating in 1 M LiTFSI DOL:DME results in growth with significantly larger average column diameters than that in carbonates, but with rough and uneven heights (Figure S8). Given that ethers

are more stable in trace amounts of water than carbonates, we hypothesized that a higher current density, and hence a higher overpotential to allow for greater electrolyte reduction, may result in greater formation of LiF and a more uniform surface. Above 4 mA cm^{-2}, the same uniformity arises. This uniformity remains until over 60 mA cm^{-2} (Figure 2), a significantly higher current density than that observed in carbonate electrolytes. When nonuniformity does occur, the entire bulk deposited film becomes rough and fibril-like (Figure S8f). At such large current densities, nonuniform growth at a single defect may propagate rapidly so there is a sudden transition relative to the more gradual transition observed in DMC. XPS point scans for the columnar growth at 4 mA cm^{-2} and the completely nonuniform growth at 60 mA cm^{-2} indicate relatively similar peaks for the F 1s and O 1s scans (Figure S8g), again indicating that loss of uniform columnar growth is not necessarily correlated with chemical inhomogeneity. The LiF peak at 688.0 eV is nearly identical, and there are only slight shifts for the Li$_2$O and Li$_2$O$_2$ peaks, with the Li$_2$O$_2$ being more dominant for the 60 mA cm^{-2} case. The nearly identical F 1s and O 1s scans are observed for the transition regions in

the FEC and DOL:DME cases, where the morphology is just starting to become nonuniform. At even higher current densities, the SEI may become chemically unstable due to electrolyte reduction at higher overpotentials vs Li. Because the transition to nonuniformity in DOL:DME occurs at such a larger current density, this may be why slight shifts in the O 1s scan are observed.

Cycling Performance in Full Cells. While the columnar diameter can be carefully controlled by choosing a substrate or applying a specific current density that results in a desired overpotential, the chemical stability of the SEI is shown to be determined by the choice of electrolyte. The stability of the SEI is not necessarily correlated with larger columns, as DMC and DMC + 10% FEC both have similarly sized diameters yet FEC clearly enhances the chemical stability. To compare the subsequent cycling efficiency of the deposited lithium, the plated films were placed in coin cells vs a delithiated $LiFePO_4$ (LFP) cathode (MTI). In this configuration, the cycling efficiency in a full cell with limited lithium content and electrolyte content can be tested, as the LFP cathode is pre-delithiated to ensure that the efficiency measurements are solely due to the columnar lithium. A proof of concept was first demonstrated by taking the 5 μm (1 mAh cm^{-2}) columns and cycling at 0.1 mA cm^{-2} for 0.2 mAh cm^{-2} (Figure 6a). It was observed that the type of substrate for deposition had a minimal effect on the cycle life, despite the variation in the columnar diameter due to the varying overpotential. The addition of 10% FEC exhibited a much greater improvement in the CE% even though the columnar diameter at the same current density and substrate was shown to be similar. Further, the XPS point scans for both electrolytes at the same current density appear to be similar. The only difference lies in the failure mode at higher current density, with 10% FEC resulting in more localized and sudden failure of the bulk lithium rather than a slow transition with growth protrusions on top of columns. The most important parameter for increasing cycle life seemed to be the amount of active lithium available; doubling the thickness to 10 μm more than doubled the cycle life, indicating that failure in both electrolyte cases is driven by rapid consumption of active lithium. Scaling up both the total amount of Li and the current rate during cycling, 30 μm columnar lithium films were deposited and subsequently cycled at 0.5 mA cm^{-2} for 1 mAh cm^{-2}, which is more representative of typical Li metal cycling protocols in the literature (Figure 6b). Similar trends were observed, with the brass substrate samples exhibiting higher coulombic efficiency than the copper or stainless steel. The cycle life of around 30–40 cycles at 0.5 mA cm^{-2} and 1 mAh cm^{-2} is comparable with literature studies of the cycling performance of commercial roll-pressed 50 μm lithium foil (China Energy Li Co.).[51]

To confirm the correlation between the amount of starting Li (thickness of columns) and cycle life, the columnar Li on copper was plated at various thicknesses (3, 4, and 6 mAh cm^{-2}) and then cycled vs LFP. Increasing the capacity of deposited Li columns (and hence the starting thickness) from 3 to 4 to 6 mAh cm^{-2} enhances the cycle life, simply because the amount of starting Li is greater, though it does not change the coulombic efficiency significantly (Figure 6c). Comparing 30 μm thick columns in DMC + 10% FEC and DOL:DME, we observe that the columns in DOL:DME are substantially thicker in diameter (>2 μm vs 150 nm), though do not necessarily exhibit improved coulombic efficiency. Other than physical growth dimensions, the SEI chemical compositions

clearly play a dominant role as they are quite different for the two electrolytes.

Lastly, the initially plated Li was subsequently stripped at various capacity intervals, followed by a second plating protocol (Figure S9). SEM images were taken at regular intervals in order to determine which portions of the columnar Li were participating in the plating/stripping behavior. It was observed that the overall thickness of Li did not change. Rather, Li from along the sides of the columns stripped off and then replated. This resulted in irregularly shaped columns, due to random portions of the sides being more electrochemically active. We suspect this is due to the spatially heterogeneous layer of SEI, causing certain portions along the columns to strip off first. This suggests that the column sides are more active than the tips, as the thickness does not change, and the columns strip off despite being further from the bulk electrolyte. For the surface growth protrusions in DMC, a similar stripping protocol showed that these protrusions did not appear to strip off, indicating the predominant presence of SEI and electrochemically inactive Li (Figure S3c). Further confirmation of columnar sides being more electrochemically active than the tips includes postmortem SEM imaging of cycled columnar Li (Figure S10). Columnar Li was deposited in 1 M LiPF$_6$ DMC + 10% FEC at various capacities (3, 4, and 6 mAh cm^{-2}) and subsequently cycled in a full cell, with cycling data shown in Figure 6c. Postmortem SEM shows that the hemispherical nuclei are still close-packed, pointing to their electrochemical inactivity. This is especially noticeable in Figure S10c,d, where the underlying columns have been mostly stripped but the surface nuclei are still completely intact. The columnar morphology can sustain after >40 cycles in a full cell at 0.5 mA cm^{-2} and 1 mAh cm^{-2} cycling protocol, due to SEI stability and preferential stripping/deposition through the underlying columnar sides. However, higher current rates such as 2 mA cm^{-2}, while capable of sustaining columnar Li in a primary deposition protocol, would present greater challenges through cycling (Figure S10e) due to loss of uniform morphology.

CONCLUSION

We report a systematic study of the factors influencing the growth and subsequent cycling performance of lithium columns deposited in three common electrolytes. First, we show that the initial nucleation and subsequent growth morphology on various substrates occurs as expected, with the substrate overpotential inversely proportional to column diameter. Second, we demonstrate via XPS 2D spatial mapping that the SEI chemical stability is linked with morphological uniformity for the DMC electrolyte, and pinpoint the origins of the chemical shifts to be localized on surface growth protrusions as observed by cryo-TEM. We then compare this with the cases of FEC and DOL:DME electrolytes, both of which show chemical stability of the SEI, specifically LiF, Li$_2$O, and Li$_2$O$_2$ inorganic species, even under the initial transition to morphological nonuniformity. Surface growth protrusions are absent. The observation of columnar growth in both carbonate and ether electrolytes, on a variety of substrate types, suggests that this uniform morphology may be an inherent growth characteristic of low current density deposition, provided a LiF-rich environment and suitable electrolyte are used. Lastly, increasing the column diameter is not necessarily correlated with improved cycling efficiency. Columns on brass substrates actually perform slightly better than columns on copper or

stainless steel, despite a larger overpotential and smaller diameters. Columns in DOL:DME perform similarly to carbonates, despite having diameters an order of magnitude larger. The cycling efficiencies, after scaling up from 5 to 30 μm at standard testing conditions of 0.5 mA cm^{-2} and 1 mAh cm^{-2}, are comparable with that of 50 μm commercial Li metal studies. Further work is in progress on understanding and optimizing the current collector and new electrolyte combinations for limited lithium content configurations. From the current study, there are initial indications that alternatives to copper substrates such as copper alloys may exhibit improved cycling efficiencies. Even more significant is the impact of the electrolyte; initial LiF-rich substrates are important, but they should be coupled with chemically stable electrolytes. Herein, we have demonstrated that primary deposition of 30 μm thick uniform Li columns can occur at 100-fold higher current densities in 1 M LiTFSI DOL:DME than in 1 M LiPF$_6$ DMC and result in Li metal quality of similar cycling efficiency.

■ METHODS

Electrochemistry. Standard 10 mL glass beaker cells were used for electrodeposition studies. Working electrodes sized 3 cm × 1 cm were prepared via a surface treatment process consisting of a 1 min immersion in oxalic acid 10% v/v, a copious rinse in deionized water, drying of bulk water on the surface using Kimwipes, and transfer into an argon filled glovebox in clean containers. The counter electrode used was a piece of lithium metal foil (Sigma-Aldrich) 750 μm thick and was cleaned with a stainless steel razor blade prior to each electrodeposition experiment. The 1 M LiPF$_6$ DMC solution was used as received (Sigma-Aldrich). Then 10% FEC by volume (Sigma-Aldrich) was added to the 1 M LiPF$_6$ DMC for the 1 M LiPF$_6$ DMC + 10% FEC electrolyte. The 1 M LiTFSI DOL:DME solution was made by dissolving the as received LiTFSI salt in DOL and DME (all Sigma-Aldrich) in a 1:1 ratio. Electrochemical experiments were carried out using a multichannel potentiostat (Ivium n-Stat) at room temperature.

Materials Characterization. A Verios 460 XHR scanning electron microscope with a quick load lock was used for the imaging of lithium deposits, with an accelerating voltage of 5 keV and a working distance of 4 mm. Each sample was rinsed in DMC and then dried in the large vacuum antechamber at 35 °C to remove residual salts. XPS analysis was performed using a Thermo Scientific K-Alpha instrument with an Al Kα source. Area scans were conducted point by point ranging from 30 to 80 μm spot size. The operating pressure was <8.0 × 10^{-8} Torr, and the sample was transferred from the argon filled glovebox via a vacuum sample holder and never exposed to atmosphere. Avantage software was used for the least-squares fitting of XPS spectra with a Lorentzian−Gaussian line shape (30% L/G mix) and a Shirley background subtraction. Etching was carried out using an argon ion gun (2 keV, monatomic, 400 μm spot size, 1 min) before each scan.

The growth asperities in 1 M LiPF$_6$ DMC were gently scraped off the underlying lithium film and directly onto a copper TEM grid with Quantifoil (R 1.2/1.3) substrate using a new stainless steel razor blade inside the glovebox. This was aided by the relatively brittle properties of the growth asperities relative to the surrounding ductile lithium film. The TEM grid was carefully mounted onto a Gatan single tilt cryo-holder inside the Ar-filled glovebox (O$_2$ < 1 ppm, H$_2$O < 0.5 ppm), and the cryo-holder was then sealed inside a vacuum bag. The vacuum bag was taken out of the glovebox and transferred immediately to the TEM characterization room, where it was cut open with shears and the cryo-holder was mounted into the TEM in less than 5 s. Once inside the TEM, it was immediately pumped down and cooled with liquid nitrogen. The sample remained stable at $T \sim$ 100 K during characterization. The TEM characterization was carried out with a Thermo Scientific Talos F200X S/TEM operated at 200 keV. The microscope was operated at low dose, as even under cryogenic conditions beam-induced degradation can be observed at high doses. The elemental analysis was conducted in S/TEM mode with SuperX-EDS, and selected area electron diffraction (SAED) was performed in TEM mode. EDS line scan resolution was approximately 2.5 nm per point. Several dendritic particles were measured for a more quantitative analysis and to determine the consistency of the observed diffraction peaks. Size measurements were done by using ImageJ software.

■ ASSOCIATED CONTENT

Ⓢ Supporting Information

The Supporting Information is available free of charge at https://pubs.acs.org/doi/10.1021/acs.chemmater.9b04385.

Additional *ex situ* SEM images and XPS mapping; TEM diffraction analysis and other cycling data (PDF)

■ AUTHOR INFORMATION

Corresponding Author

Daniel A. Steingart − *Department of Mechanical and Aerospace Engineering, Department of Chemical and Biological Engineering, and Andlinger Center for Energy and the Environment, Princeton University, Princeton, New Jersey 08540, United States; Department of Earth and Environmental Engineering, Department of Chemical Engineering, and Columbia Electrochemical Energy Center, Columbia University, New York, New York 10027, United States;* ⬤ orcid.org/0000-0002-8184-9641; Email: dan.steingart@columbia.edu

Authors

Wesley Chang − *Department of Mechanical and Aerospace Engineering and Andlinger Center for Energy and the Environment, Princeton University, Princeton, New Jersey 08540, United States; Department of Chemical Engineering and Columbia Electrochemical Energy Center, Columbia University, New York, New York 10027, United States;* ⬤ orcid.org/0000-0002-9389-1265

Jeung Hun Park − *Department of Mechanical and Aerospace Engineering, Department of Chemical and Biological Engineering, and Andlinger Center for Energy and the Environment, Princeton University, Princeton, New Jersey 08540, United States; Department of Chemical Engineering, Columbia University, New York, New York 10027, United States*

Nikita S. Dutta − *Department of Mechanical and Aerospace Engineering, Princeton University, Princeton, New Jersey 08540, United States;* ⬤ orcid.org/0000-0003-2301-4010

Craig B. Arnold − *Department of Mechanical and Aerospace Engineering, Department of Chemical and Biological Engineering, and Andlinger Center for Energy and the Environment, Princeton University, Princeton, New Jersey 08540, United States*

Complete contact information is available at:
https://pubs.acs.org/10.1021/acs.chemmater.9b04385

Author Contributions

W.C. designed the experiments, conducted the electrochemical and characterization experiments, and wrote the manuscript. N.D. conducted the cryo-TEM characterization. J.H.P. carried out the TEM diffraction analysis. D.S. supervised the project.

Notes

The authors declare no competing financial interest.

■ REFERENCES

(1) Choi, J. W.; Aurbach, D. Promise and Reality of Post-Lithium-Ion Batteries with High Energy Densities. *Nat. Rev. Mater.* **2016**, *1*, 16013.

(2) Xu, W.; Wang, J.; Ding, F.; Chen, X.; Nasybulin, E.; Zhang, Y.; Zhang, J.-G. Lithium Metal Anodes for Rechargeable Batteries. *Energy Environ. Sci.* **2014**, *7* (2), 513−537.

(3) Zhang, J. G.; Xu, W.; Henderson, W. A. Lithium Metal Anodes and Rechargeable Lithium Metal Batteries. *Springer Ser. Mater. Sci.* **2017**, *249*, 1−194.

(4) Liu, B.; Zhang, J. G.; Xu, W. Advancing Lithium Metal Batteries. *Joule* **2018**, *2* (5), 833−845.

(5) Winter, M.; Barnett, B.; Xu, K. Before Li Ion Batteries. *Chem. Rev.* **2018**, *118* (23), 11433−11456.

(6) Albertus, P.; Babinec, S.; Litzelman, S.; Newman, A. Status and Challenges in Enabling the Lithium Metal Electrode for High-Energy and Low-Cost Rechargeable Batteries. *Nature Energy* **2018**, *3* (1), 16−21.

(7) Liu, J.; Bao, Z.; Cui, Y.; Dufek, E. J.; Goodenough, J. B.; Khalifah, P.; Li, Q.; Liaw, B. Y.; Liu, P.; Manthiram, A.; et al. Pathways for Practical High-Energy Long-Cycling Lithium Metal Batteries. *Nature Energy* **2019**, *4* (3), 180−186.

(8) Mashtalir, O.; Nguyen, M.; Bodoin, E.; Swonger, L.; O'Brien, S. P. High-Purity Lithium Metal Films from Aqueous Mineral Solutions. *ACS Omega* **2018**, *3* (1), 181−187.

(9) Chang, W.; Park, J. H.; Steingart, D. A. Poor Man's Atomic Layer Deposition of LiF for Additive-Free Growth of Lithium Columns. *Nano Lett.* **2018**, *18* (11), 7066−7074.

(10) Snydacker, D. H. US 2018/0133619 A1, 2018. Retrieved from: http://www.freepatentsonline.com/20180133619.pdf.

(11) Genovese, M.; Louli, A. J.; Weber, R.; Hames, S.; Dahn, J. R. Measuring the Coulombic Efficiency of Lithium Metal Cycling in Anode-Free Lithium Metal Batteries. *J. Electrochem. Soc.* **2018**, *165* (14), A3321−A3325.

(12) Qian, J.; Adams, B. D.; Zheng, J.; Xu, W.; Henderson, W. A.; Wang, J.; Bowden, M. E.; Xu, S.; Hu, J.; Zhang, J. G. Anode-Free Rechargeable Lithium Metal Batteries. *Adv. Funct. Mater.* **2016**, *26* (39), 7094−7102.

(13) Lin, D.; Liu, Y.; Cui, Y. Reviving the Lithium Metal Anode for High-Energy Batteries. *Nat. Nanotechnol.* **2017**, *12* (3), 194−206.

(14) Pei, A.; Zheng, G.; Shi, F.; Li, Y.; Cui, Y. Nanoscale Nucleation and Growth of Electrodeposited Lithium Metal. *Nano Lett.* **2017**, *17* (2), 1132−1139.

(15) Zhang, Y.; Qian, J.; Xu, W.; Russell, S. M.; Chen, X.; Nasybulin, E.; Bhattacharya, P.; Engelhard, M. H.; Mei, D.; Cao, R.; et al. Dendrite-Free Lithium Deposition with Self-Aligned Nanorod Structure. *Nano Lett.* **2014**, *14* (12), 6889−6896.

(16) Ren, X.; Zhang, Y.; Engelhard, M. H.; Li, Q.; Zhang, J. G.; Xu, W. Guided Lithium Metal Deposition and Improved Lithium Coulombic Efficiency through Synergistic Effects of LiAsF6and Cyclic Carbonate Additives. *ACS Energy Lett.* **2018**, *3* (1), 14−19.

(17) Zhang, X. Q.; Chen, X.; Xu, R.; Cheng, X. B.; Peng, H. J.; Zhang, R.; Huang, J. Q.; Zhang, Q. Columnar Lithium Metal Anodes. *Angew. Chem., Int. Ed.* **2017**, *56* (45), 14207−14211.

(18) Kanamura, K. Electrochemical Deposition of Very Smooth Lithium Using Nonaqueous Electrolytes Containing HF. *J. Electrochem. Soc.* **1996**, *143* (7), 2187.

(19) Choudhury, S.; Archer, L. A. Lithium Fluoride Additives for Stable Cycling of Lithium Batteries at High Current Densities. *Advanced Electronic Materials* **2016**, *2* (2), 1500246.

(20) Tikekar, M. D.; Choudhury, S.; Tu, Z.; Archer, L. A. Design Principles for Electrolytes and Interfaces for Stable Lithium-Metal Batteries. *Nature Energy* **2016**, *1* (9), 1−7.

(21) Cheng, X. B.; Zhang, R.; Zhao, C. Z.; Zhang, Q. Toward Safe Lithium Metal Anode in Rechargeable Batteries: A Review. *Chem. Rev.* **2017**, *117* (15), 10403−10473.

(22) Ko, J.; Yoon, Y. S. Recent Progress in LiF Materials for Safe Lithium Metal Anode of Rechargeable Batteries: Is LiF the Key to Commercializing Li Metal Batteries? *Ceram. Int.* **2019**, *45* (1), 30−49.

(23) Zhang, X. Q.; Cheng, X. B.; Chen, X.; Yan, C.; Zhang, Q. Fluoroethylene Carbonate Additives to Render Uniform Li Deposits in Lithium Metal Batteries. *Adv. Funct. Mater.* **2017**, *27* (10), 1605989.

(24) Yu, H.; Zhao, J.; Ben, L.; Zhan, Y.; Wu, Y.; Huang, X. Dendrite-Free Lithium Deposition with Self-Aligned Columnar Structure in a Carbonate-Ether Mixed Electrolyte. *ACS Energy Lett.* **2017**, *2* (6), 1296−1302.

(25) Wang, C.; Meng, Y. S.; Xu, K. Perspective—Fluorinating Interphases. *J. Electrochem. Soc.* **2019**, *166* (3), A5184−A5186.

(26) Yan, K.; Lu, Z.; Lee, H. W.; Xiong, F.; Hsu, P. C.; Li, Y.; Zhao, J.; Chu, S.; Cui, Y. Selective Deposition and Stable Encapsulation of Lithium through Heterogeneous Seeded Growth. *Nature Energy* **2016**, *1* (3), 1−5.

(27) Wood, K. N.; Teeter, G. XPS on Li-Battery-Related Compounds: Analysis of Inorganic SEI Phases and a Methodology for Charge Correction. *ACS Appl. Energy Mater.* **2018**, *1* (9), 4493−4504.

(28) Etacheri, V.; Marom, R.; Elazari, R.; Salitra, G.; Aurbach, D. Challenges in the Development of Advanced Li-Ion Batteries: A Review. *Energy Environ. Sci.* **2011**, *4* (9), 3243−3262.

(29) Lin, D.; Liu, Y.; Li, Y.; Li, Y.; Pei, A.; Xie, J.; Huang, W.; Cui, Y. Fast Galvanic Lithium Corrosion Involving a Kirkendall-Type Mechanism. *Nat. Chem.* **2019**, *11*, 382.

(30) Pelton, A. D. The Cu-Li (Copper-Lithium) System. *Bull. Alloy Phase Diagrams* **1986**, *7* (2), 142−144.

(31) Li, W.; Yao, H.; Yan, K.; Zheng, G.; Liang, Z.; Chiang, Y. M.; Cui, Y. The Synergetic Effect of Lithium Polysulfide and Lithium Nitrate to Prevent Lithium Dendrite Growth. *Nat. Commun.* **2015**, *6* (May), 1−8.

(32) Zhang, D.; Dai, A.; Wu, M.; Shen, K.; Xiao, T.; Hou, G.; Lu, J.; Tang, Y. Lithiophilic 3D Porous CuZn Current Collector for Stable Lithium-Metal Batteries. *ACS Energy Lett.* **2020**, *5*, 180−186.

(33) Huang, S.; Zhang, W.; Ming, H.; Cao, G.; Fan, L.-Z.; Zhang, H. Chemical Energy Release Driven Lithiophilic Layer on 1 m2 Commercial Brass Mesh towards Highly Stable Lithium Metal Batteries. *Nano Lett.* **2019**, *19*, 1832.

(34) Tu, Z.; Choudhury, S.; Zachman, M. J.; Wei, S.; Zhang, K.; Kourkoutis, L. F.; Archer, L. A. Designing Artificial Solid-Electrolyte Interphases for Single-Ion and High-Efficiency Transport in Batteries. *Joule* **2017**, *1* (2), 394−406.

(35) Xu, K. Electrolytes and Interphases in Li-Ion Batteries and beyond. *Chem. Rev.* **2014**, *114* (23), 11503−11618.

(36) Zachman, M. J.; Tu, Z.; Choudhury, S.; Archer, L. A.; Kourkoutis, L. F. Cryo-STEM Mapping of Solid-liquid Interfaces and Dendrites in Lithium-Metal Batteries. *Nature* **2018**, *560* (7718), 345−349.

(37) Peled, E.; Menkin, S. SEI: Past, Present and Future. *J. Electrochem. Soc.* **2017**, *164*, A1703.

(38) Tang, M.; Albertus, P.; Newman, J. Two-Dimensional Modeling of Lithium Deposition during Cell Charging. *J. Electrochem. Soc.* **2009**, *156* (5), A390.

(39) Qian, J.; Henderson, W. A.; Xu, W.; Bhattacharya, P.; Engelhard, M.; Borodin, O.; Zhang, J.-G. High Rate and Stable Cycling of Lithium Metal Anode. *Nat. Commun.* **2015**, *6*, 6362.

(40) Wood, K. N.; Noked, M.; Dasgupta, N. P. Lithium Metal Anodes: Toward an Improved Understanding of Coupled Morphological, Electrochemical, and Mechanical Behavior. *ACS Energy Lett.* **2017**, *2* (3), 664−672.

(41) Nie, M.; Lucht, B. L. Role of Lithium Salt on Solid Electrolyte Interface (SEI) Formation and Structure in Lithium Ion Batteries Role of Lithium Salt on Solid Electrolyte Interface (SEI) Formation. *J. Electrochem. Soc.* **2014**, *161*, A1001.

(42) Jurng, S.; Brown, Z. L.; Kim, J.; Lucht, B. L. Effect of Electrolyte on the Nanostructure of the Solid Electrolyte Interphase (SEI) and Performance of Lithium Metal Anodes. *Energy Environ. Sci.* **2018**, *11*, 2600−2608.

(43) Wang, X.; Zhang, M.; Alvarado, J.; Wang, S.; Sina, M.; Lu, B.; Bouwer, J.; Xu, W.; Xiao, J.; Zhang, J. G.; et al. New Insights on the Structure of Electrochemically Deposited Lithium Metal and Its Solid Electrolyte Interphases via Cryogenic TEM. *Nano Lett.* **2017**, *17* (12), 7606−7612.

(44) Li, Y.; Huang, W.; Li, Y.; Pei, A.; Boyle, D. T.; Cui, Y. Correlating Structure and Function of Battery Interphases at Atomic Resolution Using Cryoelectron Microscopy Correlating Structure and Function of Battery Interphases at Atomic Resolution Using Cryoelectron Microscopy. *Joule* **2018**, *2*, 2167.

(45) Huang, W.; Boyle, D. T.; Li, Y.; Li, Y.; Pei, A.; Chen, H.; Cui, Y. Nanostructural and Electrochemical Evolution of the Solid-Electrolyte Interphase on CuO Nanowires Revealed by Cryogenic-Electron Microscopy and Impedance Spectroscopy. *ACS Nano* **2019**, *13* (1), 737−744.

(46) Li, Y.; Li, Y.; Pei, A.; Yan, K.; Sun, Y.; Wu, C. L.; et al. Atomic Structure of Sensitive Battery Materials and Interfaces Revealed by Cryo-electron Microscopy. *Science* **2017**, *358* (6362), 506−510.

(47) Han, S. Y.; Boebinger, M. G.; Kondekar, N. P.; Worthy, T. J.; Mcdowell, M. T. Seeded Nanowire and Microwire Growth from Lithium Alloys Seeded Nanowire and Microwire Growth from Lithium Alloys. *Nano Lett.* **2018**, *18*, 4331.

(48) Bai, P.; Li, J.; Brushett, F. R.; Bazant, M. Z. Transition of Lithium Growth Mechanisms in Liquid Electrolytes. *Energy Environ. Sci.* **2016**, *9* (10), 3221−3229.

(49) Yamaki, J. I.; Tobishima, S. I.; Hayashi, K.; Saito, K.; Nemoto, Y.; Arakawa, M. A Consideration of the Morphology of Electrochemically Deposited Lithium in an Organic Electrolyte. *J. Power Sources* **1998**, *74* (2), 219−227.

(50) Steiger, J.; Kramer, D.; Mönig, R. Mechanisms of Dendritic Growth Investigated by in Situ Light Microscopy during Electrodeposition and Dissolution of Lithium. *J. Power Sources* **2014**, *261*, 112−119.

(51) Chen, S.; Niu, C.; Lee, H.; Li, Q.; Yu, L.; Xu, W.; Zhang, J. G.; Dufek, E. J.; Whittingham, M. S.; Meng, S.; et al. Critical Parameters for Evaluating Coin Cells and Pouch Cells of Rechargeable Li-Metal Batteries. *Joule* **2019**, *3* (4), 1094−1105.